Effects of the chemical states of N sites and mesoporosity of N-doped carbon supports on single-atom Ru catalysts during CO_2-to-formate conversion

Kwangho Park [a],[1], Kyung Rok Lee [a],[1], Sunghee Ahn [a],[b],[1], Canh Van Nguyen [a],[b], Kwang-Deog Jung [a],[b],[*]

[a] Clean Energy Research Center, Korea Institute of Science and Technology, 5, Hwarang-ro 14-gil, Seongbuk-gu, Seoul 02792, Republic of Korea
[b] Division of Energy & Environmental Technology, KIST school, Korea University of Science and Technology, Seoul 02792, Republic of Korea

ARTICLE INFO

ABSTRACT

This study explores the fabrication and characterization of mesoporous nitrogen-doped carbon replicas (MNCs) as Ru catalyst supports for CO_2 hydrogenation to formate. MNC supports with a cubic Ia3d-like structure were successfully synthesized from a KIT-6 template. The mesoporosity, N content, and N states in the MNCs differed according to the precursor type, which substantially influenced the stability of single-atom Ru catalysts during CO_2 conversion. In hydrogenation tests, the Ru/MNC prepared using acrylonitrile precursor (Ru/MNC-A) demonstrated the best stability, whereas the Ru/MNCs prepared using pyrrole and melamine exhibited low activity owing to Ru agglomeration and limited reactant diffusion, respectively. The excellent stability of Ru/MNC-A resulted from Ru migration and rearrangement, as evidenced by near edge X-ray absorption fine structure analyses. Ru/MNC-A and Ru/MNC-A-400 achieved an outstanding turnover number of 69,000 in CO_2 hydrogenation over 72 h. Remarkably, the Ru/MNC-A catalyst demonstrated exceptional stability, attaining a TON of 315,840 over 360 h.

1. Introduction

Single-atom catalysts (SACs) supported on functionalized porous solid materials are of great significance owing to their excellent catalytic performance in the hydrogenation of CO_2 to formic acid, which is not only considered a promising liquid organic hydrogen carrier but also a sustainable platform chemical [1–3]. Many studies have elucidated that the improved catalytic activities of supported SACs are due to the unique electronic and structural characteristics of the metal as well as the promotional effect of the support on the catalytic performance [4]. Explorations into the addition of heteroatoms on the support materials or other second single metal at the SAC sites have been conducted intensively, revealing that such modifications can substantially alter catalyst ability, notably reactivity and selectivity, by fostering distinct

interactions with the host material or inducing an alloying effect [5–7]. However, the reductive and harsh conditions of the hydrogenation process can cause the isolated SACs to agglomerate into nanoparticles. In addition, the supported SACs can leach out of the catalyst body during hydrogenation, especially during continuous flow reactions. Therefore, inducing a strong interaction between the metal species and support is desirable to maintain the original dispersed state of the SACs during the reaction. As the dispersion and stability of the SACs on the support are significantly dependent on the geometrical and chemical characteristics of the support, achieving precise control over the physical and chemical properties of the catalyst support has been a significant challenge for decades.

Recently, certain emerging porous materials, such as covalent triazine frameworks (CTFs) and porous organic polymers (POPs), have

sparked interest as relevant catalyst supports for stabilizing the SACs even under the reductive conditions of CO_2 hydrogenation to produce formic acid. This has been viable due to the presence of well-defined and strong metal-anchoring sites on the skeletal structure of the porous support, the geometrical and chemical properties of which can be strategically altered by the meticulous choice of building blocks [8–18]. However, the primitive CTF and POP supports possess a microporous structure with less than 2 nm pore size, which can be a limiting barrier for the mass transfer of the reactants to the catalytically active sites. To increase the porosity of the support structures, thermal treatment at a high temperature is conducted or a linker unit with a unique 3D structure, which is difficult to synthesize, is used in the synthesis. In particular, pyridinic N sites, which are known to be strong metal-binding groups, on the support are more vulnerable and decompose under the thermal-treatment condition compared to others, such as pyrrolic and graphitic N, which in turn weaken the metal-anchoring capacity of the support [19,20].

Various synthetic approaches have been explored to overcome the threshold for the efficient mass transfer of the reactants to catalytic sites by rendering the support mesoporous and also simultaneously incorporating multifunctional ligands in the support [21–23]. For instance, Gascon et al. reported a molecular Ir catalyst supported on CTF coated on a cordierite monolith with a macroporous structure and high surface area to implement a higher level of porosity in the Ir@CTF/polymer sphere composite [24,25]. Yamashita et al. reported a molecular Ir catalyst anchored on iminophosphine-ligand incorporated polyethyleneimine, denoted as Ir-PN-PEI, which was subsequently anchored on the surface of titanium nanotubes with a high surface area and large pore size (~6 nm) [26]. Recently, Copéret et al. developed Ru and Ir molecular catalysts supported on pincer-ligand-tethered SBA-15 and a silica bead support that readily facilitated the hydrogenation of CO_2 to formate [27,28]. Despite these promising studies, the complexity of the synthetic steps of the catalyst preparation impedes the scale-up of the synthetic process. Furthermore, the deactivation of the catalysts during recycling and long-term hydrogenation processes poses another significant challenge to be overcome for improving the catalyst performance.

Nanocasting is a well-known method for fabricating mesoporous carbon replicas with precisely controlled textural characteristics derived from the template and the chemical composition of the skeletal body [29,30]. Therefore, nanocasted materials have attracted significant interest as relevant catalyst supports that not only facilitate the diffusion of the reactants and products but also provide strong anchoring sites for the SACs. Recently, Shen et al. reported co-catalyst systems of Ir SACs and nanoparticles supported on a CMK-3 support; these catalysts were produced by the nanocasting method using SBA-15 as the template and sucrose as the precursor [31]. Zhang et al. reported the in situ generation of Cu SACs supported on mesoporous N-doped carbon materials using SBA-15 as the hard template and dopamine as the precursor [32]. Both the SAC-based catalytic systems exhibited promising activities and stabilities in hydrogenation and oxidative coupling reactions. Despite these prominent studies, nanocasted mesoporous supports have been rarely employed for anchoring CO_2 hydrogenation catalysts, and only a limited number of investigations have unveiled the significant role of the support.

In this study, we employed KIT-6, which is composed of a cubic bicontinuous silica mesostructure with a high surface area and narrow pore size distribution, as a hard template to fabricate a support with a highly ordered mesoporous structure. Specifically, we focus on strategies for designing stable SACs, wherein our research introduces nitrogen dopants known for their strong binding capabilities to the SACs. To achieve this, we have conducted an preliminary investigation and judiciously selected carbon/nitrogen precursors that would yield different chemical states of N atoms, such as pyridinic N and graphitic N, after the calcination process on nano-coated support materials (Supplementary text and Fig. S1). Consequently, the catalyst synthesized using acrylonitrile as a precursor (Ru/MNC-A) produced with a well-

defined 3D mesoporous structure and high nitrogen content shows substantial catalytic activity and stability. We demonstrate that this stem from the unique characteristic of the Ru SACs stably bound to the support material by the strong interaction even under the reductive conditions. Utilizing advanced analytical techniques such as HAADF-STEM, accelerator-based EXAFS, and NEXAFS for precise identification of catalytic active sites has been crucial for the analysis on SAC-based catalytic system. Furthermore, DFT calculations have been instrumental in clarifying the optimal structure and outstanding stability of SAC-based active sites. This research provides novel insights into the optimal structure and composition of catalysts for effective CO_2 conversion into formic acid, a valuable chemical.

2. Experimental section

2.1. Materials

Anhydrous iron(III) chloride ($FeCl_3$, 97%), pyrrole (98%), acrylonitrile (99%), monomethyl ether hydroquinone remover, melamine (99%), formaldehyde (37% with 10–15 wt% methanol as a stabilizer), hydrofluoric acid (HF, 48%), and sulfuric acid (99%) were purchased from Sigma-Aldrich and used without further purification. Aqueous HCl (2 N) and ammonia (28–30 wt%) solutions, ethanol (99%), and triethylamine (TEA, 99%) were procured from Samchun Pure Chemical Company, Republic of Korea. 4,4′-Azobisisobutyronitrile was obtained from Junsei Company, Japan. Double-distilled water was used in all experiments. All the gases (99.99% in purity) used in this study were supplied by Shinyang Company, Republic of Korea.

2.2. Preparation of KIT-6

The modification method of procedure by Kim et al. was utilized to produce KIT-6, cubic ordered mesoporous silica [30]. The composition of the components was the same as in the reported process (TEOS:P123: HCl:H_2O:n-BuOH = 1:0.017:1.83:195:1.31 in mole ratio), but a 2 HCl solution was used instead of a concentrated HCl solution (35 wt%). First, 6.0 g of P123 was added to a mixture of 60 mL of 2 N HCl and 160 mL of water. The resulting mixture was stored overnight to ensure the complete dissolution of P123 and the formation of a micellar structure. Next, 6.0 g of n-butanol was added to the micellar solution under vigorous stirring at 35 °C over 1 h, followed by 12.8 g of TEOS, and the resulting mixture was stirred for 24 h. Then, the final mixture was transferred to a propylene bottle and rapidly heated to 100 °C in an oven under static conditions. After 24 h at 100 °C, the closed bottle was cooled to 25 °C. The solid product was collected by filtration and washed with a large amount of water. The template was removed by thermal treatment (calcination) at 550 °C for 6 h (ramp rate: 2 °C·min^{-1}). Finally, KIT-6 was obtained at > 90% yield and characterized to be a highly ordered mesoporous structure (Fig. S1 and S2).

2.3. Preparation of MNCs and Ru/MNCs

A series of MNCs was prepared using pyrrole, acrylonitrile, and melamine as carbon/nitrogen precursors, and the resulting samples are denoted as MNC-P, MNC-A, and MNC-M, respectively. The final carbonization of all the MNC materials was carried out at 800 °C with a ramping rate of 2 °C·min^{-1} under nitrogen flow (100 mL·min^{-1}).

MNC-P. KIT-6 (1.0 g) was infiltrated with a solution of $FeCl_3$ (1.2 g) dissolved in 1 mL of ethanol. After drying the sample in a vacuum oven at 80 °C, 0.6 mL of pyrrole was introduced to the dried iron chloride/ silica composite, facilitating the polymerization of pyrrole within the pores. The mixture was cured at 350 °C for 2 h (ramp rate: 5 °C·min^{-1}). After cooling to 25 °C, the procedure was repeated for the second polymerization of pyrrole using 0.6 g of iron chloride in 0.5 mL of ethanol and then adding 0.25 mL of pyrrole. The sample was again cured similarly to the first step, followed by final carbonization.

MNC-A. KIT-6 (1.0 g) was mixed with 1 mL of a solution containing the radical initiator, 4,4′-azobisisobutyronitrile (3 wt%) in acrylonitrile (with removed inhibitor). The polymerization of acrylonitrile was carried out at 60 °C for 24 h. The polymer/silica composite underwent curing at 250 °C for 2 h, then was heated to 350 °C for another 2 h (2 °C·min^{-1}). A second infiltration used 0.8 mL of the acrylonitrile/ radical initiator solution. The resulting mixture underwent annealing first at 250 °C for 2 h, and then at 350 °C for 2 h, preceding the final carbonization.

MNC-M. KIT-6 (1.0 g) was dispersed with a solution containing melamine (1.0 g), ethanol (5.0 mL), formaldehyde (1.8 mL), and 28 wt% aqueous ammonia (0.5 mL). The solution was stirred at 65 °C for 30 min in a sealed vial to produce methylol melamine. Solvent evaporation was done at 65 °C in an oil bath in a fume hood. The collected solid sample was then processed in an alumina boat and cured at 140 °C for 5 h under nitrogen. This was followed by the final carbonization step.

MC-S. KIT-6 (1.0 g) was mixed with a solution of sucrose (1.25 g), sulfuric acid (0.14 g), and water (5 mL). The mixture was dried in a vacuum oven at 100 °C and subsequently treated at 160 °C for 6 h. After cooling to 25 °C, the procedure was repeated using a new solution of 0.8 g of sucrose, 0.09 g of sulfuric acid, and 5 mL of water. This sample was then cured at 160 °C for 6 h, followed by the final carbonization.

Silica etching. After carbonization, the silica template was removed by dissolution in a diluted HF solution. In detail, 1.0 g of KIT-6 was suspended in a mixture of water, ethanol, and concentrated HF (48%) at 1:1:1 vol ratio. The resulting mixture was stirred vigorously for 2 h, filtered, and then washed with abundant amounts of water and acetone. For preparing MNC-P, the 2 N HCl solution was utilized instead of water to effectively wash out FeCl$_3$.

Metallization. The mesoporous N-doped carbon replica (200 mg) was dispersed in 32 mL of methanol, and then 8 mL of a ruthenium solution (Ru content: 0.5 mg·mL^{-1}) was added to the mixture. The metallization of the Ru was conducted under reflux for 24 h. The reaction mixture was cooled to 25 °C, and the ruthenium-containing carbon was collected by filtration, washed with methanol and acetone, and finally dried overnight under vacuum at 80 °C.

2.4. Characterization

Small-angle X-ray scattering (SAXS) data were obtained in the range of $2\theta = 0.045$–3° using a Nanopi instrument from Rigaku equipped with a Cu Kα radiation source (1.2 kW, $\lambda = 1.5418$ Å). Wide-angle X-ray diffraction (XRD) patterns were collected from a Bruker instrument (D8 advance) using Cu Kα radiation and a Ni filter at 40 kV and 40 mA in the 2θ range of 10 to 70° at a scanning rate of 3°·min^{-1}. A surface area analysis instrument (BELSORP mini II and BELSORP max, Japan) was used to obtain the nitrogen adsorption–desorption isotherms of the materials at 77 K. The surface area of the material was calculated using the Bruanuer–Emmett–Teller (BET) equation in the P/P_0 region of 0.05–0.3. Pore-size distribution was evaluated using non-local density function theory (NLDFT) by assuming a cylindrical shape for silica and slit-pore model for carbon replica. Raman spectra were collected with a Renishaw CCD Camera using a 532 nm Ar laser excitation source. X-ray photoelectron spectroscopy (XPS; PHI 5000 VersaProbe) was performed using monochromatic Al Kα radiation (1486.6 eV) under ultra-high vacuum (2.0×10^{-7} Pa). Before collecting the XPS profiles, the material surface was cleaned by Ar-ion sputtering. The XPS peaks were calibrated with respect to the signal of adventitious carbon at 284.6 eV. The contents of carbon, nitrogen, oxygen, and hydrogen were determined using an elemental analyzer (Thermo Scientific FLASH 2000). High-resolution transmission electron microscopy (HR-TEM) and scanning transmission electron microscopy (STEM) was conducted on a double Cs-corrected Titan Themis transmission electron microscope (FEI, TitanTM 80–300). The ruthenium content of materials was analyzed by inductively coupled plasma optical emission spectrometry (ICP-OES; iCAP6000 Series, Thermo Scientific). High-performance

liquid chromatography (HPLC) was conducted using a YL instrument (YL 9100 Plus) to evaluate the formic acid concentration after the reaction. X-ray absorption spectra: X-ray absorption fine structure (XAFS) spectra were collected using the 8 C Nano XAFS, 10 C Wide XAFS and near edge X-ray absorption fine structure (NEXAFS) spectra were collected using the 10D XAS Korea Institute of Science and Technology beamlines of the Pohang Accelerator Laboratory (PLS-II, 3.0 GeV, South Korea). The acquired XAFS data was treated by using Demeter 0.9.26. For the EXAFS fitting, S_0^2 value of 0.82 was opt to calculate the coordination number for each bonding component. H$_2$ temperature programmed reduction (H$_2$-TPR) was conducted on a BELCAT II (BEL JAPAN INC.). We used a carrier gas composed of a 5% H$_2$/Ar mixture, flowing at 30 mL·min^{-1}, and the temperature increased from 40 to 650 °C at a rate of 10 °C·min^{-1}. Before starting the test, the sample was dried for an hour at 150 °C using an argon flow.

2.5. Catalytic activity measurement

Typically, 60 mg of the catalyst was transferred to a batch reactor with 40 mL of a 1 M TEA solution. After assembling the reactor, CO$_2$ and H$_2$ were consecutively fed into the batch reactor up to pressures of 80 bar with 1:1 ratio at 25 °C. The temperature was increased up to 120 °C over 30 min, and then the reaction was carried out at the stirring rate of 300 rpm for 2 h. Thereafter, the reactor was cooled rapidly to 25 °C using a fan. The liquid product was collected through a 0.2 μm filter paper. The formate concentration was determined by conducing HPLC using 5 mM H$_2$SO$_4$ solution as the eluent. In addition, mole of Ru contained in the prepared catalysts was determined based on the Ru content in the catalyst quantified by ICP-OES analysis.

TON = mole of HCOOH/mole of Ru

Turnover frequency (TOF) (h^{-1})= TON/reaction time (h)

2.6. Catalyst recycle test

Initially, 60 mg of the catalyst was used in the reaction, and the reaction was performed as described in Section 2.5. After every cycle, the catalyst was collected by filtration and washed with an 250 mL of water and 250 mL of acetone to remove the residual products and TEA. Then, the cleaned catalyst was dried overnight in a vacuum drying oven at 80 °C, and was employed to the next recycle test.

2.7. Time dependent catalytic activity measurement

Initially, we added 10 mg of the chosen catalyst to a reactor filled with 60 mL of a 3 M TEA solution, aiming for a high substrate-to-catalyst ratio. As the reaction progressed over time, we periodically collected liquid product samples through a line fitted with a micro-filter. These products were later identified using HPLC analysis.

2.8. Density functional theory calculation

Spin-polarized density functional theory calculations were conducted to understand the catalytic behavior of the Ru single atom catalyst supported on the prepared NDC using the Vienna ab initio simulation package (VASP 6.2.0). The core electron of each atom is expressed with the projector-augmented wave method. The electron exchange-correlation energy was described using the generalized gradient approximation (GGA) with the Perdew-Burke-Ernzerhof functional. The van der Waals interaction was treated using the DFT+D3 approach with the Becke-Johnson damping function. Each simulation's optimization was performed with a cutoff energy of 400 eV. Convergence of electronic and ionic relaxations was achieved when each value was below 10^{-5} eV and 0.05 eV/Å, respectively. A $3 \times 3 \times 1$ gamma-centered k-point grid

was adopted for k-space integration. The vacuum thickness was set to 20 Å in the z-direction to ignore the interaction between the upper and lower simulated structures. The adsorption energy of Ru single atom on each surface, E_{abs}, was calculated as follow;

$$E_{abs} = E_{Ru-surface} - E_{Ru} - E_{surface}$$

Where the $E_{Ru\text{-}surface}$, E_{Ru}, and $E_{surface}$ indicate the calculated total energy of adsorbed Ru system, isolated Ru in vacuum cell, and prepared surface, respectively. The reaction pathway and relative energy at each reaction coordinate was investigate by the climbing image nudged elastic band (CI-NEB) method, and the spring constant was set at -5.0 eV/Å². The activation energy was determined as the difference between the lowest and highest relative energy.

3. Results and discussion

As illustrated in Fig. 1, MNCs were fabricated via the nanocasting method using different types of N-containing carbon precursors, such as pyrrole, melamine, and acrylonitrile. As a reference sample, a mesoporous carbon replica (MC-S) devoid of nitrogen was prepared using sucrose as the precursor. The HR-TEM images in Fig. 2a–c confirm the successful formation of mesoporous structures in the synthesized MNC-A, MNC-P, and MC-S supports. The mesoporous structure exhibited high regularity and an approximate pore size of 4 nm. In contrast, the TEM image of MNC-M prepared using melamine as the precursor did not display the distinct ordered mesoporous structure; instead, it revealed an amorphous structure (Fig. 2d). These characteristics were further substantiated through SAXS analysis. The SAXS profiles of MNC-A, MNC-P, and MC-S in Fig. 2e exhibit strong reflection peaks at 2θ of $1.1°$ and $1.3°$, corresponding to the (211) and (220) reflection of cubic $ia3d$ phase in an accordance with the SAXS profile of KIT-6 (Fig. S3) [33], whereas the SAXS profile of MNC-M exhibits no discernible peaks. These results suggest that MNC-A, MNC-P, and MC-S effectively formed a replica structure with cubic Ia3d symmetry via inverse transcription from KIT-6, the hard template, but an ordered mesoporous structure was not properly generated in MNC-M.

The nitrogen sorption isotherms of the synthesized materials are shown in Fig. 2f. A common feature observed for all carbon replica samples was an uptake starting at P/P_0 values above 0.4, which indicates the presence of a mesoporous structure [34]. The BET surface areas of MC-S, MNC-P, MNC-A, and MNC-M are 1089, 934, 724, and 1152 m²·g⁻¹, respectively (Table S1). NLDFT was employed to determine the pore-size distribution (PSD) of the MNCs, and the results are presented in Fig. 2g. The PSD curves of MC-S indicate the presence of mesopore structure with pore widths of 3.7 nm corroborating the TEM results. The smaller pore widths compared to the pore wall thickness of the KIT-6 template (4.3 nm) suggest carbon shrinkage during synthesis (Table S2) [35]. For MNC-P and MNC-A, larger pore sizes were found in the PSD at 5.8 and 5.6 nm, respectively, which may be attributed to several factors, such as the partial incomplete filling of the pore structure by the precursor. In addition, void spaces can form after the dissolution of iron species in the MNC-P sample [36,37]. In contrast, the PSD curve of MNC-M displayed pore widths at 2.4 nm, signifying a strong prevalence of a microporous structure. This observation is further supported by the pore volume analysis of the MNC materials using the t-plot method. The calculated micropore and mesopore volumes for each sample are presented in Table S1. Notably, MNC-M exhibited a dominant presence of micropore volume, while the other samples primarily demonstrated mesopore volumes as the major component. These findings support the hypothesis that the type of precursor used in the synthesis can readily modulate the pore size of the support.

The microstructures of the carbon supports were further examined through wide-angle XRD analysis. As depicted in Fig. 3a, all the XRD patterns feature broad and low-intensity peaks at 2θ values of $\sim23°$ and $42°$, corresponding to the (002) and (100) planes of carbon, respectively (circle). The distinct strong peaks of MNC-P observed at 2θ values of $\sim26°$ and $53°$ (diamond), corresponding to the (002) and (004) planes of graphitic carbon generated by the presence of iron species during carbonization [38,39]. Accordingly, the Raman spectra exhibited an increasing trend in the D to G band ratio, following the order of MC-S (D/G = 0.87), MNC-P (D/G = 1.05), MNC-A (D/G = 1.14), and MNC-M (D/G = 1.45) (Fig. 3b and Table S3). This observation indicates an increase in the amorphous character due to the incorporation of N dopants into the carbon replica structure.

Table S4 illustrates the elemental composition of the supports, as determined by elemental analysis. The obtained data highlight the distinct nitrogen contents of the MNCs, with the N contents of MNC-M, MNC-A, and MNC-P being 23.96, 13.70, and 3.10 wt%. Furthermore,
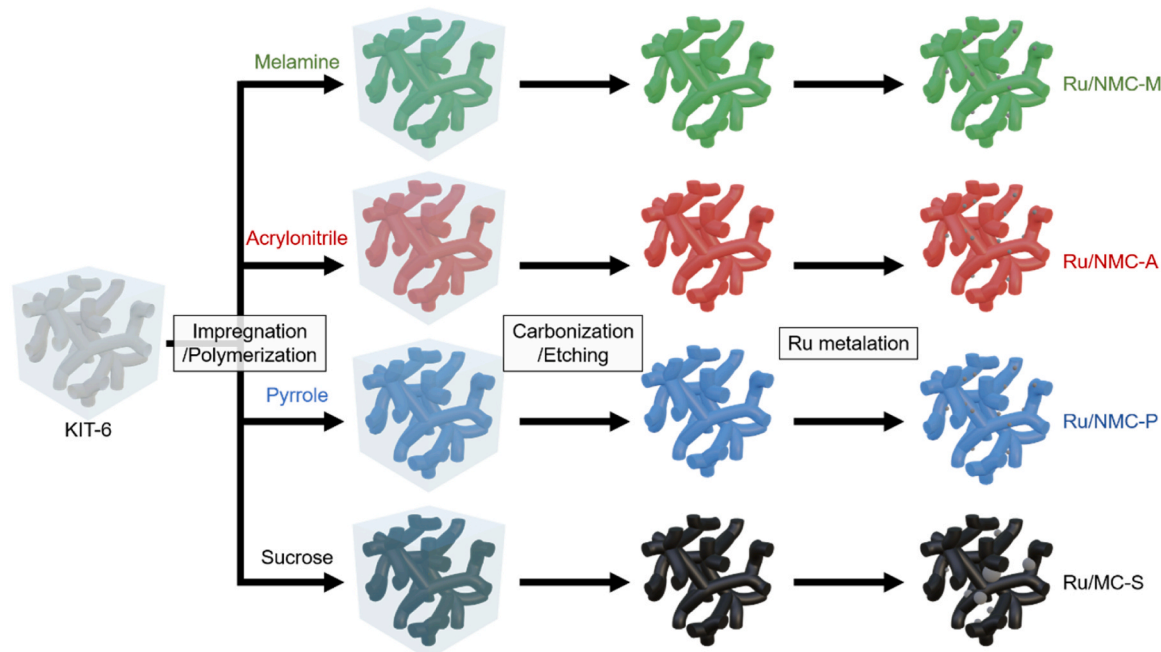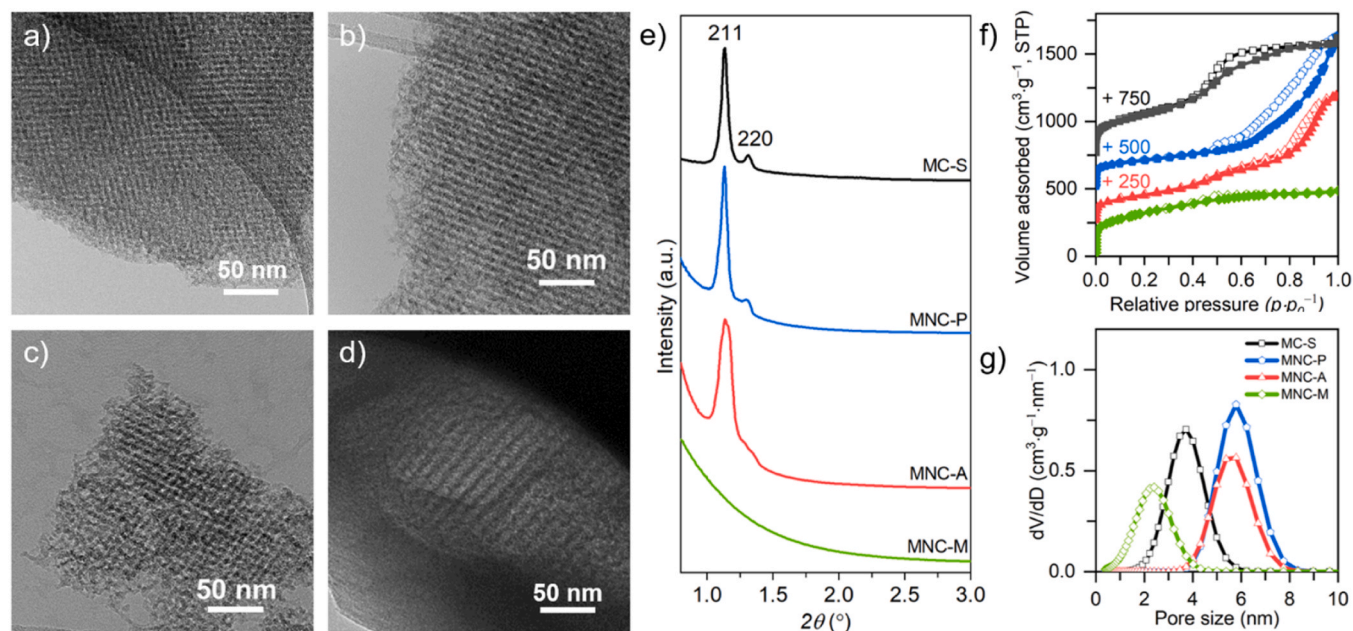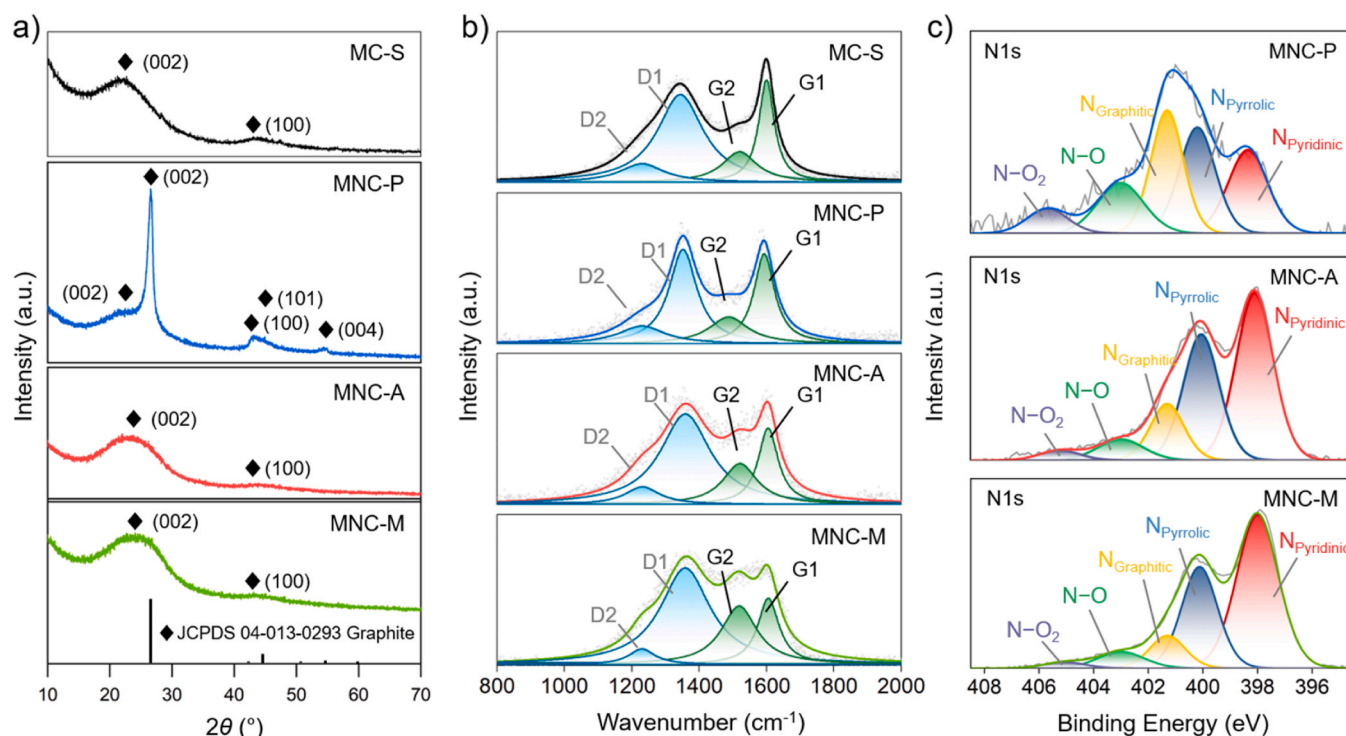

Fig. 1. Schematic representation of the synthesis of Ru/MNC catalysts.

Fig. 2. HR-TEM images of MC-S (a), MNC-P (b), MNC-A (c), and MNC-M (d). SAXS patterns of the as-prepared MNCs and MC-S (e). N_2 adsorption–desorption isotherms (solid: adsorption, open: desorption) (f) and NLDFT pore-size distribution (g) of carbon replicas.

Fig. 3. Characterization of MNCs and MC-S supports: XRD patterns (a), Raman spectra (b), and deconvoluted N 1 s XPS profiles of the MNCs.

the N 1 s XPS profiles of the MNCs could be deconvoluted into five distinct peaks, corresponding to pyridinic N (398–398.6 eV), pyrrolic N (400–400.5 eV), graphitic N (401–401.5 eV), N-O (403–403.8 eV), and N-O_2 (404.5–405 eV) species (Fig. 3c). A prominent presence of pyridinic N species was observed for MNC-M and MNC-A, whereas graphitic N was found to be the dominant species in MNC-P (Table S5). These analyses underscore the distinct nitrogen contents and chemical states of N sites present in the MNCs, which are influenced by the choice of precursor.

Ru species were immobilized on the synthesized supports using a wet chemical process with a methanolic solution of RuCl$_3\cdot$xH$_2$O, resulting in Ru/MNC-M, Ru/MNC-A, Ru/MNC-P, and Ru/MC-S catalysts. ICP-OES analysis was performed to confirm the initial Ru loading in the prepared catalysts. Considering the target Ru loading of 2 wt%, the results revealed that the MNC-M support had the highest Ru-carrying capacity of 1.90 wt%. This was followed by MNC-A (1.61 wt%), MNC-P (1.04 wt%), and MC-S (0.15 wt%) (Table S6). These findings indicate the variable Ru-loading capacity of the different supports, with MNC-M being

the most effective in accommodating the targeted Ru content. Moreover, this trend aligned with the nitrogen content of the supports determined by elemental analysis, suggesting that N dopants play a crucial role in the immobilization of Ru species. Nonetheless, the Ru/MC-S catalyst was deemed unsuitable for further investigation owing to its significantly low metal content. Therefore, Ru/MC-S-im was prepared using the impregnation method to evaluate the changes in the catalyst properties and performance during pretreatment and hydrogenation reactions, and the Ru content of Ru/MC-S-im was determined to be 1.92 wt%.

High-angle annular dark-field STEM (HAADF-STEM) analysis was conducted to evaluate the dispersion of the supported Ru species in the as-prepared catalysts. A higher proportion of Ru aggregates was observed in Ru/MC-S-im without N dopants, as shown in Fig. 4a. In contrast, the TEM images in Fig. 4b–d reveal the dispersion of isolated Ru atoms in the Ru/MNC-P, Ru/MNC-A, and Ru/MNC-M catalysts, highlighting the essential role of N sites in immobilizing the Ru SACs owing to their strong metal-binding capability. The XPS profiles in Fig. 5a demonstrate that the Ru 3 $P_{3/2}$ core-level regions of the Ru/MNC catalysts display a peak in the 463.23–464.50 eV range which closely resembles the peak observed for the RuCl$_3$·xH$_2$O precursor at 464.10 eV [40]. This similarity indicates that the supported Ru species maintained

their Ru^{3+} oxidation state. Furthermore, it suggests that the electron density of the Ru atoms in the catalysts increased due to charge transfer from the N sites, after Ru-N coordination occurred. To more precisely validate the electronic and structural features of the Ru species in the Ru/MNC catalysts, Ru K-edge X-ray absorption spectroscopy was performed. As shown in Fig. 5b, the X-ray absorption near-edge structure (XANES) spectra illustrate that the energy absorption threshold for the Ru/MNCs is lower than that of RuO$_2$, yet it surpasses the threshold for both Ru foil and RuCl$_3$·xH$_2$O. This particular observation corroborates that the oxidation state of the supported Ru species falls between Ru^{3+} and Ru^{4+}. For a more comprehensive understanding of the structural details, the extended X-ray absorption fine structure (EXAFS) spectra of Ru are shown in Fig. 5c. The radial distances determined for Ru, corresponding to Ru-Ru, Ru-O, and Ru-Cl interactions, are 2.5, 1.6, and 1.9 Å, respectively. These values are consistent with the results obtained for Ru foil (2.5 Å), RuO$_2$ (1.6 Å), and RuCl$_3$ (2.0 Å). The consistent Ru radial distance of 1.9 Å observed for all Ru/MNC-A samples (Ru-Cl distance is 1.9 Å) suggests that Ru-Cl represents the dominant Ru species on the MNC supports. Furthermore, the cumulative peak of Ru-N and Ru-O coordination appears as a broad pattern for all samples, with the corresponding bond length being ~1.6 Å. Notably, a discernible metallic Ru-Ru scattering peak is conspicuously absent in the profile of
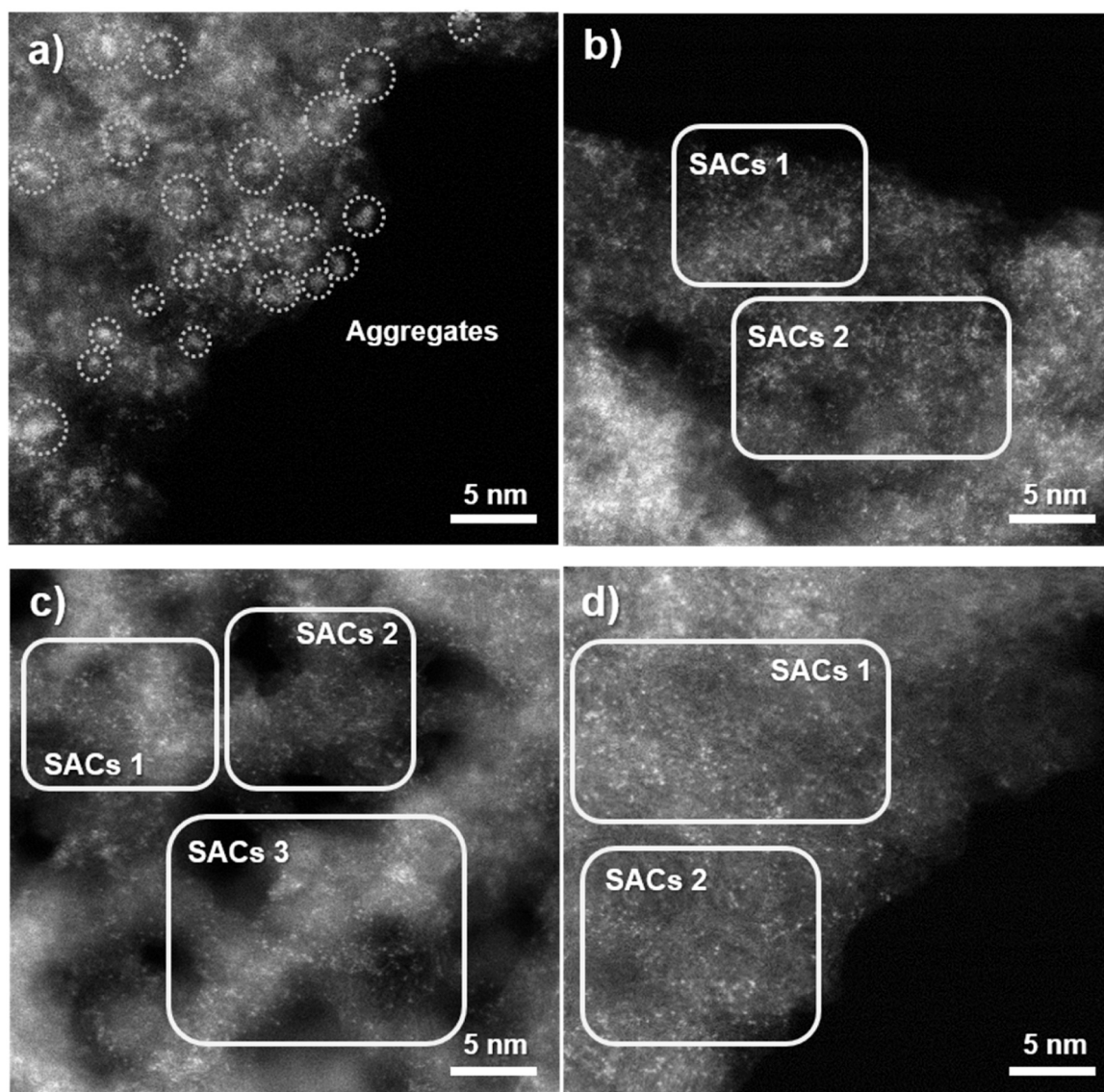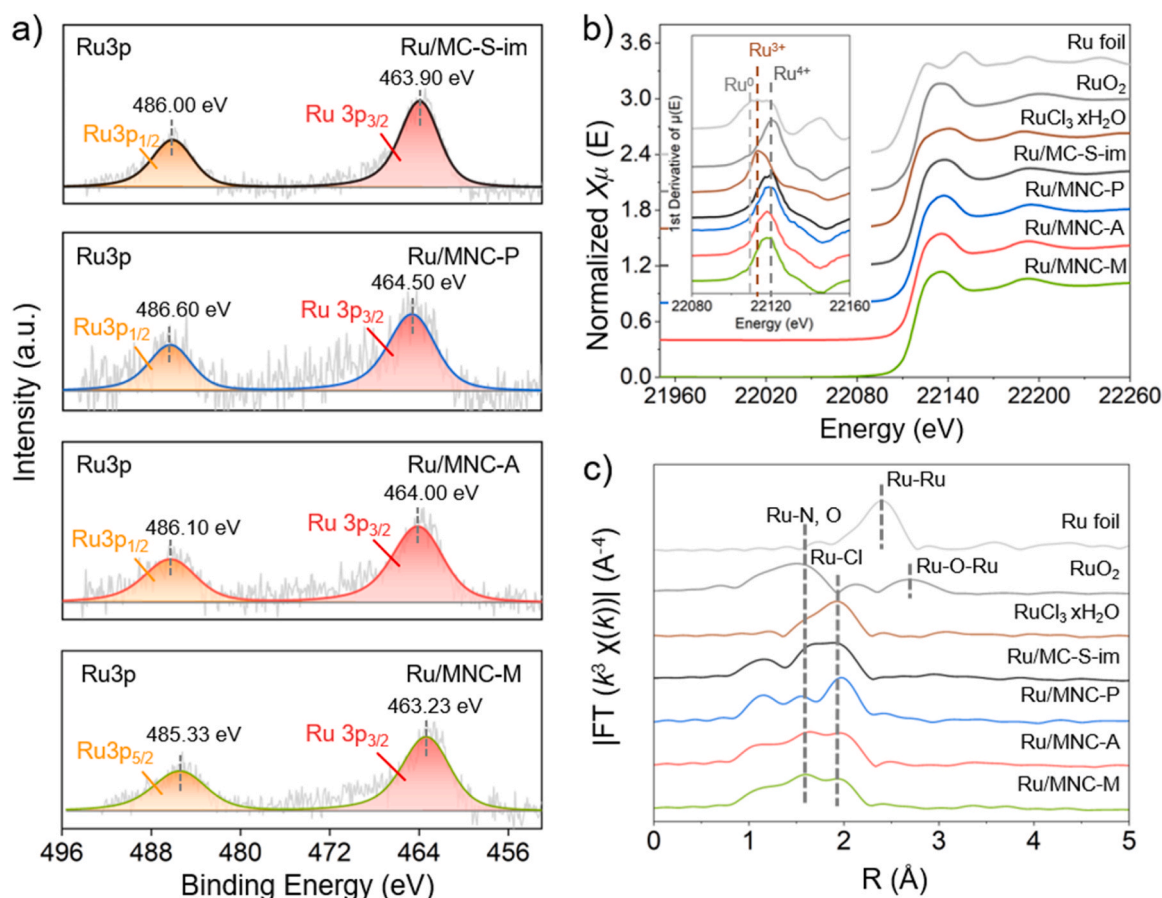

Fig. 4. HAADF-STEM images of Ru/MC-S-im (a), Ru/MNC-P (b), Ru/MNC-A (c), and Ru/MNC-M (d).

Fig. 5. Spectroscopic characterization of Ru/MNCs and Ru/MC-S-im. Deconvoluted Ru 3p spectra (a), normalized Ru K-edge XANES spectra (b) and first derivative of the Ru K-edge XANES (inset), and FT EXAFS spectra (c) of Ru/MNCs and Ru/MC-S-im.

each supported Ru catalyst, implying that Ru species are dispersed at the atomic scale on the support. Further, according to the fitting by using Ru-N and Ru-Cl contribution (Fig. S5 and Table S8), the coordination numbers for the Ru/MNC-A were determined to be 3.03 for Ru-N and 3.18 for Ru-Cl. This result indicates the presence of the strong interaction of Ru SACs on the surface of MNC-A support with Ru-3 N configuration. In the case of fresh Ru/MNC-M, the CN values were calculated to be 3.3 for Ru-N and 2.8 for Ru-Cl bonds. Fresh Ru/MNC-P showed CN of 2.58 for Ru-N and 3.02 for Ru-Cl bonds. Fresh Ru/MC-S-im exhibited a lower CN of 1.8 for Ru-O bonds and 3 for Ru-Cl bonds, indicating a weak interaction between the Ru and the support material.

The hydrogenation of CO_2 to formate was examined under batch conditions at 120 °C and 8 MPa (under ambient conditions) using the as-synthesized catalysts (Table 1). The initial catalytic activity was quantified using the TOF, which represents the number of formate molecules produced per mole of Ru atom in the catalyst per hour. Before evaluating the catalytic activity, a series of control experiments was performed to understand the explicit roles of the different components. Primarily, the catalytic activities of the support and Ru precursor were assessed. The synthesized supports without Ru yielded negligible conversion (Table S9) and $RuCl_3 \cdot xH_2O$ showed a poor catalytic conversion with a TOF of 200 h^{-1}. These results indicate that Ru is the catalytically active component, but the Ru precursor itself does not efficiently catalyze the hydrogenation of CO_2. This is because although $RuCl_3 \cdot xH_2O$ was completely dissolved in the solvent before the reaction, the dissolved Ru species precipitated as yellowish particles during the hydrogenation reaction owing to their reduction (Fig. S6). Further, the preliminary tests conducted without water and TEA resulted in a very low conversion of CO_2 to formate, indicating their key roles in the hydrogenation reaction, such as the stabilization of the reactants and products in the form of

Table 1

Assessment of the initial catalytic activities of Ru/MNCs and reference experiments[a].

Sample	Ru content[b] (wt%)	[FA][c] (mol L^{-1})	TON[d]	TOF[e] (h^{-1})
$RuCl_3 \cdot xH_2O$[f]	-	0.080	400[f]	200
Ru/N-doped graphene	1.55	0.313	1360	680
Ru/MNC-P	1.04	0.530	3430	1715
Ru/MNC-A	1.61	0.743	3120	1560
Ru/MNC-M	1.90	0.152	540	270
Ru/MC-S-im	1.92	0.571	2000	1000
Ru/MNC-A[g]	1.61	0.007	-	-
Ru/MNC-A[h]	1.61	0.005	-	-

[a]Reaction conditions for typical reactions, which employed 60 mg of the catalyst in 40 mL of a 1 M aqueous TEA solution for 2 h at a stirring rate of 500 rpm. The initial pressure was increased to 8.0 MPa at 25 °C with a H_2/CO_2 ratio of 1:1 and then increased further to 11.0–11.8 MPa at 120 °C. [b]The Ru content was determined through ICP-OES analysis, and [c]the formate concentration was determined via high-performance liquid chromatography. [d]TON is defined as $mole_{FA}/mole_{Ru}$, and [e]TOF is TON divided by the reaction time. [c–e]These values are averages from three batch reactions. [f]Hydrogenation with the use of 1.65 mg of the $RuCl_3 \cdot xH_2O$ precursor. [g]One set of batch reaction exclusively utilized pure H_2O as a solvent, [h]whereas the other set was operated under neat conditions using TEA as the solvent.

bicarbonate and formate adducts (Table 1).

In contrast, the supported Ru catalysts of Ru/MNC-P and Ru/MNC-A exhibited TOF values of 1715 and 1560 h^{-1}, respectively, indicating a significant enhancement relative to the activity of the Ru precursor. As corroborated by the characterization results, the improved catalytic activities of the supported Ru catalysts can be ascribed to their high

dispersity owing to the N-dopants in the support. The activities of our catalysts are comparable to those of Ru SACs immobilized on N-doped carbon supports in prior studies [16,17]. However, despite the high metal content and distinct single-atomic dispersion state of the Ru species, the Ru/MNC-M catalyst demonstrated a significantly low catalytic activity, exhibiting a TOF of only 270 h^{-1}. Considering the results from the N$_2$ physisorption and PSD analysis, MNC-M has a predominantly microporous structure with low regularity of the mesoporous structure. Thus, its low activity can be ascribed to the limited diffusion of reactants to the active Ru species during the hydrogenation reaction. Moreover, the low activity of Ru/MC-S-im with a TOF of 1000 h^{-1} is ascribed to a lower proportion of the dispersed active Ru species owing to Ru aggregation as shown in the TEM analysis. As a control experiment, the activity of the CO$_2$ conversion reaction was tested using a Ru catalyst supported on N-doped graphene, with the detailed characterization of this catalyst provided in the Fig. S7, S8 and Table S10. Upon subjecting this catalyst to hydrogenation under the optimal conditions established for our reaction, it achieved a TON of 1360. This performance is notably lower compared to the catalysts based on the replica structure, underscoring again the pivotal role of the mesoporous support structure in influencing catalytic activity.

To evaluate the recyclability of the catalysts, a series of hydrogenation experiments were performed under optimized conditions (Fig. 6). After each reaction cycle, the catalyst was retrieved via filtration and reused after washing and drying under vacuum. The specific activities of the synthesized Ru catalysts were determined by considering the number of formate molecules generated per unit weight of the recovered catalyst (mmol$_{FA}$·g$_{cat}^{-1}$) (Fig. 6, left y axis). Following this, the relative specific activity, denoted as the specific activity at a particular cycle relative to that in the first cycle, was calculated to evaluate the recyclability of the catalyst. Ru/MNC-A demonstrated promising stability and maintained 55.8% of the initial activity after the fifth cycle. Ru/MNC-M showed a slightly lower recyclability, retaining 51.4% of its initial activity after the fifth cycle, whereas Ru/MNC-P exhibited a more noticeable decrease in catalytic conversion, retaining only 20.2% of its initial activity after the fifth cycle. The non-nitrogen-doped Ru/MC-S

catalyst demonstrated a drastic reduction in specific activity, followed by complete deactivation after the third run.

To elucidate the underlying cause of the observed decline in the catalytic activity during the recycling experiment, the catalysts recovered after the fifth run were characterized comprehensively. An in-depth structural analysis of the MNC supports confirmed that neither the porosity nor the chemical state of N had changed discernibly (Fig. S9-14 and Table S12). In addition, ICP-OES was performed to analyze the Ru concentration in the filtrate over successive recycling cycles to rigorously track the potential Ru leaching from the catalyst (Fig. 6, right y axis). Throughout the recycling tests, a marginal reduction in the Ru content was observed for Ru/MNC-A, from the initial value of 1.61 wt% to 1.50 wt%, implying ~93% retention of the original Ru content. Similarly, Ru/MNC-M and Ru/MNC-P demonstrated a slight depletion of the Ru content (1.90 to 1.75 wt% for Ru/MNC-M (~92.1% retention of the initial content) and 1.04 to 0.92 wt% for Ru/MNC-P (~89.4% retention)). Notably, Ru/MC-S-im displayed significant Ru leaching, which was evident even after the second run. These findings underscore the vital role played by the N species in the support material in mitigating the leaching of the Ru species during the hydrogenation reaction. Taking into account the amount of Ru retained in the catalyst, the average TOF (TOF$_{avg}$) of Ru/MNC-A and Ru/MNC-M was subsequently computed to be 940 and 150 h^{-1} in the fifth run, respectively, indicating a TOF decrease of 60% and 56%, respectively, with respect to the first run. Ru/MNC-P demonstrated a TOF value of 388 h^{-1} in the fifth run, representing 20% of the initial TOF.

Changes in the dispersion state of the supported Ru species were observed through STEM. Ru metal species could be rarely observed in the used Ru/MC-S-im, suggesting that significant Ru leaching occurred during the reaction (Fig. 7a). In contrast, a large number of metal nanoparticles was identified in spent Ru/MNC-P (Fig. 7b). The d-spacing of the lattice fringe was determined to be 0.22 nm through FFT analysis of the HR-STEM image; this d-spacing corresponds to the (200) plane of the metallic Ru structure. Remarkably, the Ru/MNC-A catalyst sufficiently maintained the initial state of Ru SACs without any noticeable agglomeration of Ru even after the reaction (Fig. 7c). In contrast, in the
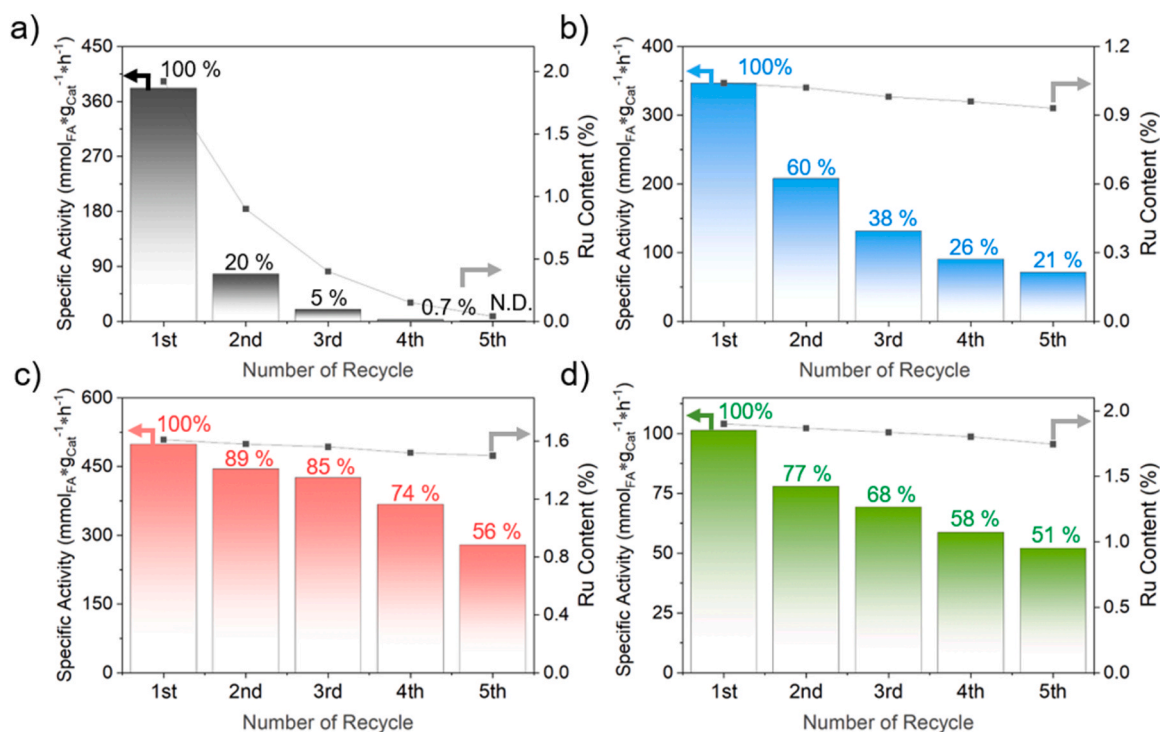
Fig. 6. Recyclability tests: specific catalytic activity (column), relative specific activity (column top), and estimated Ru content (dot and line) in Ru/MC-S-im (black), Ru/MNC-P (blue), Ru/MNC-A (red), and Ru/MNC-M (green).
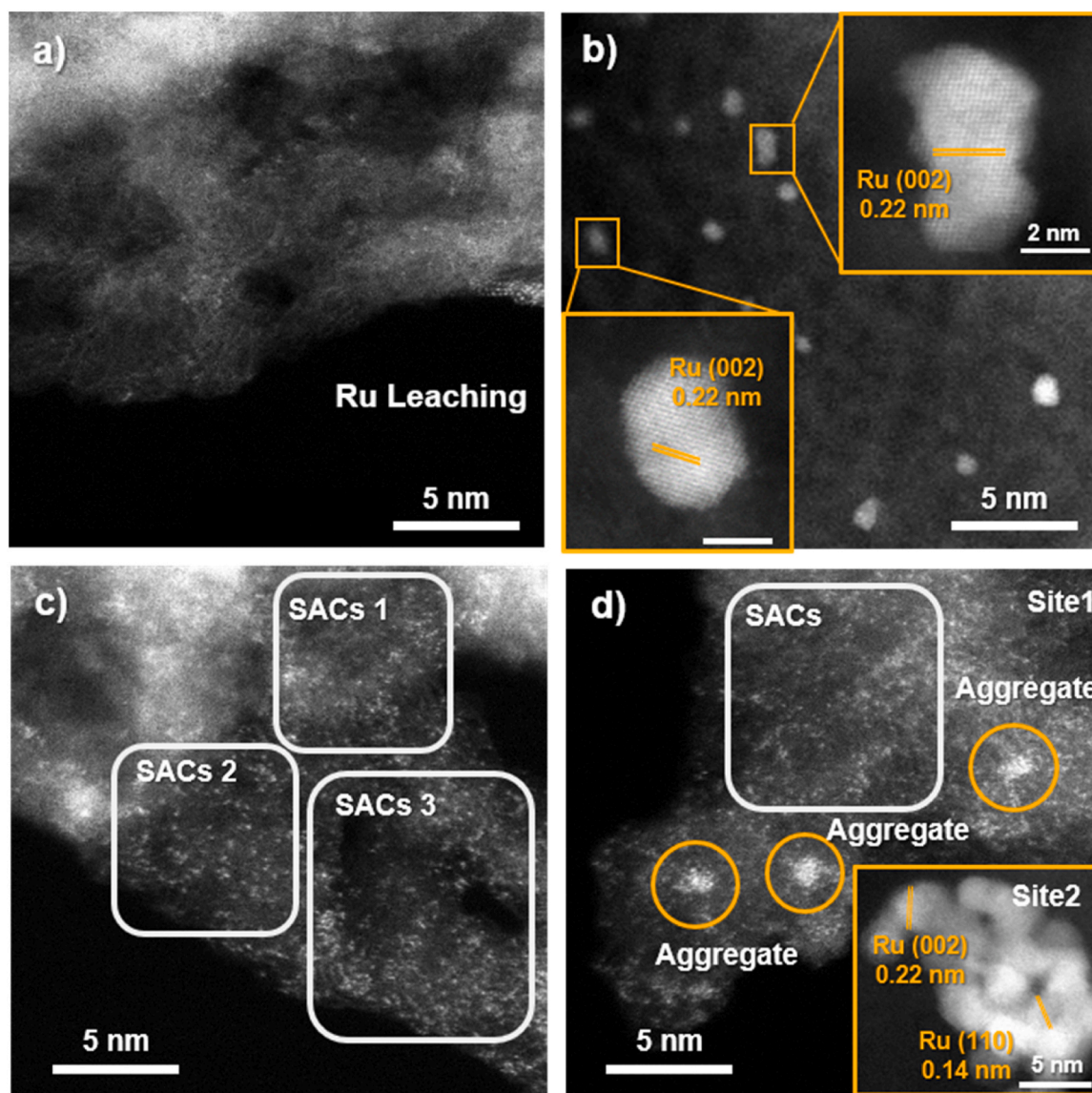
Fig. 7. HAADF-STEM images of spent Ru/MC-S-im (a), spent Ru/MNC-P (b), spent Ru/MNC-A (c), and spent Ru/MNC-M (d).

MNC-M catalyst, the Ru SACs were stably maintained in some portions of the catalyst surface (Fig. 7d, inset of site 1), but the aggregation of SACs into nanoparticles was observed on other portions (Fig. 7d, inset of site 2). FFT analysis confirmed that the two discernible *d*-spacing of the lattice fringes were 0.22 and 0.14 nm, which correspond to the (002) and (110) planes of metallic Ru, respectively.

The atomic components of the recovered catalysts were analyzed using XPS (Fig. 8a). The deconvoluted Ru 3p XPS profile of Ru/MNC-A exhibited a peak corresponding to Ru $3p_{3/2}$ at 463.90 eV, indicating that the oxidation state of Ru was stably maintained at 3 +. This result suggests that the single atomic state of Ru was well preserved in the catalyst. In contrast, the deconvoluted Ru 3p XPS profile of the spent Ru/MNC-M revealed that the Ru binding energy shifted to a lower value of 463.00 eV. This demonstrates that a significant portion of the Ru species was reduced during the reaction, corroborating the formation of Ru nanoparticles, as observed in the TEM images. Further, Cl was not detected in the recovered catalysts, indicating that Cl was easily substituted during reactions (Fig. S15). However, an accurate analysis of the spent Ru/MNC-P and Ru/MC-S-im catalysts could not be conducted using XPS, as the content of the Ru species in the recovered catalysts was low.

The XAS analysis of the spent catalysts reveal insightful information about their local coordination properties exhibiting excellent sensitivity at lower Ru content. XANES spectra reveal that the energy absorption threshold for the spent Ru/MNCs remains similarly situated compared to those of fresh catalysts, suggesting that the oxidation state of the Ru remains stable and retained after the reaction. In the EXAFS spectrum of spent Ru/MNC-A, a bond distance of 1.6 Å was maintained, indicating the presence of Ru-N bonds, and the intensity of the Ru-Cl bond (1.9 Å) was significantly decreased. Additionally, the Ru-Ru bond distance (2.3 Å) remained almost unchanged, confirming the maintenance of a stable SAC state. Analysis of the curve fitting on the EXAFS spectra for the spent Ru/MNC-A revealed a Ru-N coordination number of 3.00, with no discernible contributions from Ru-Cl or Ru-Ru bonds (Fig. S16 and Table S8). For Ru/MNC-M, the peak corresponding to the Ru-Ru bond (2.3 Å) became intense, and a clear peak appeared at 2.6 Å for the Ru-O-Ru bond distance, indicating the formation of bulk RuO_x. This is speculated to be the result of RuO_2 formation upon exposure to air, along with the severe reduction of the Ru species in the Ru/MNC-M catalyst during the reaction. The curve fitting of the EXAFS spectra for the used Ru/MNC-M indicated a Ru-N coordination number of 3.75, and the presence of Ru-Ru and Ru-O-Ru bonds was observed with coordination
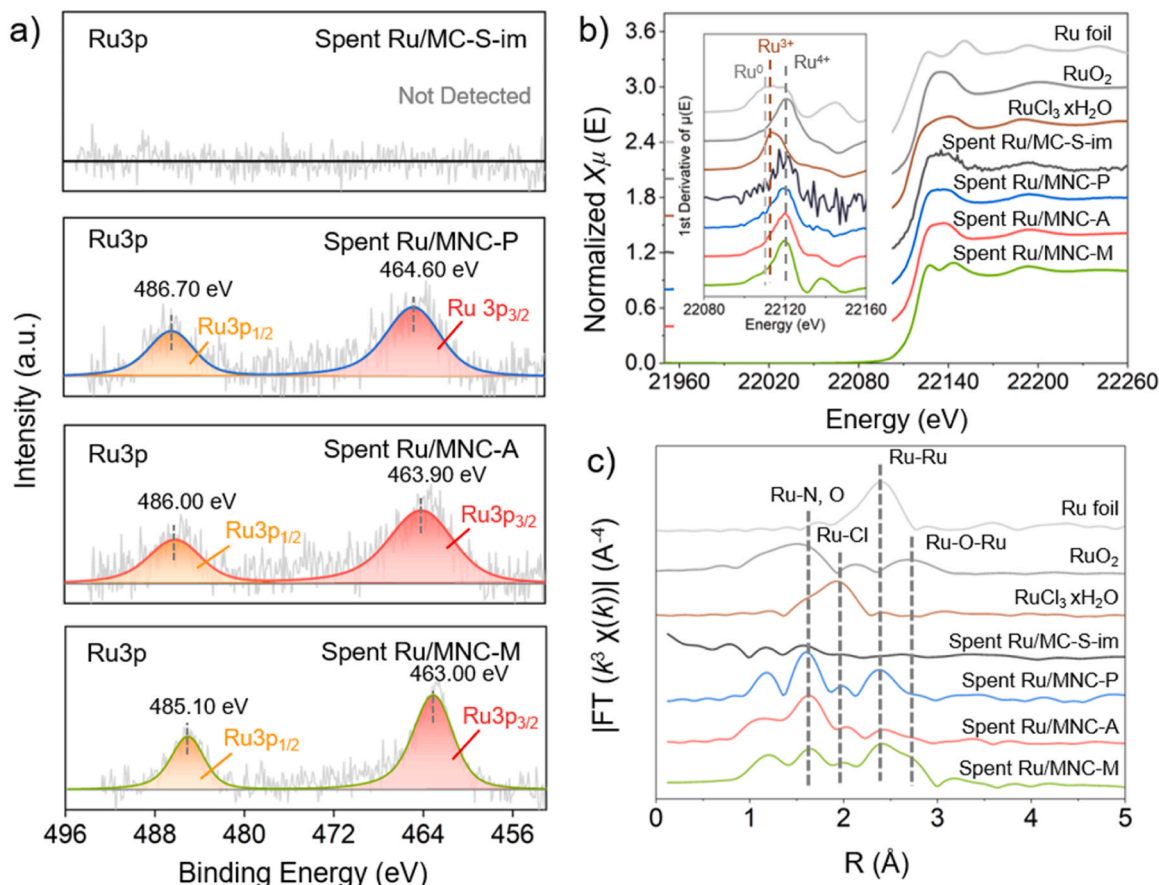
Fig. 8. Spectroscopic characterization of spent Ru/MNCs. Deconvoluted Ru 3p spectra (a), normalized Ru K-edge XANES spectra (b), and first derivative of the Ru K-edge XANES (inset), and FT EXAFS profiles (c) of spent Ru MNCs.

numbers of 9.00 and 0.40, respectively (Fig. S16 and Table S8). In the case of the spent Ru/MNC-P catalyst, bond distances were determined at 1.9 Å for Ru-N with a coordination number of 3.75, and at 2.3 Å for Ru-Ru with a coordination number of 1.98. This suggests the formation of Ru-Ru bonds, indicative of substantial nanoparticle development. The spent Ru/MC-S-im displayed no identifiable coordination peak, which is a consequence of the substantial depletion of the remaining Ru content caused by severe leaching during the hydrogenation process.

A detailed analysis of the aforementioned experimental outcomes reveals a close correlation between the stability of the Ru SACs and the pore structure of the support and the chemical state of nitrogen dopants. For Ru/MNC-M, despite the strong interaction between the Ru SACs and MNC-M support, the poorly developed pore structure of the support exposes the Ru SACs, thereby making them susceptible to reduction and oxidation by the external environment. This results in the rapid loss of the Ru SAC properties. The Ru/MNC-P catalyst also exhibited a notable decline in the activity during hydrogenation because of the intense agglomeration of the Ru SACs owing to weak binding interactions between the Ru SACs and graphitic N sites. Similarly, the Ru/MNC-S-im catalyst underwent severe agglomeration and leaching of Ru species during the recycling tests owing to weak interaction with the support.

Among the various catalysts, Ru/MNC-A demonstrated a significantly greater stability and maintained the Ru SAC property, resisting leaching and agglomeration during the hydrogenation. This is marked by its high nitrogen content, predominance of the pyridinic N sites, and a well-formed 3D mesoporous structure. Thus, the activity decrease observed during the recycling tests of Ru/MNC-A could not be attributed to the changes in the intrinsic characteristics of the support or Ru SAC. Instead, we anticipated changes in the local coordination environment around the Ru SAC under the reducing conditions. Therefore, to

determine the underlying cause of the activity decrease, we performed a detailed analysis of the behavior of Ru/MNC-A under reducing conditions.

First, to understand the redox property of the Ru SACs in the Ru/MNC-A catalyst, we conducted a TPR analysis (Fig. S17). The results revealed that the reduction of the loaded Ru started at ~130 °C and was completed at ~400 °C. Consequently, in further experiments, in addition to studying pristine and spent Ru/MNC-A catalysts, we synthesized additional catalysts to investigate the changes in the state of Ru/MNC-A under various reducing conditions. The additional catalysts were synthesized through preliminary heat treatment and are denoted as Ru/MNC-A-200, 300, and 400, according to the calcination temperature.

To analyze the characteristics of the local coordination of the catalytic active sites, we conducted a NEXAFS study. Fig. 9 presents the NEXAFS spectra at the N K-edge for the synthesized Ru/MNC-A catalysts, exhibiting four prominent absorption peaks. The three peaks at the photon energies of 399.3, 400.5, and 402.2 eV in the spectrum can be attributed to the electronic transitions of the N 1 s electron to the vacant πN 2p molecular orbitals of pyridinic N, pyrrolic N, and graphitic N, respectively [41]. The broader peak observed at the photon energy of 408.0 eV is due to the transition of the N 1 s electron to the empty σN 2p molecular orbitals of the N species. Comparing the spectra of the Ru/MNC-A catalysts with the MNC-A support, we observed a heightened intensity of absorption resonances, demonstrating direct interactions between N dopants and Ru species.

Notably, as the calcination temperature increased, an evident increase in the absorption resonance intensities of pyridinic N and pyrrolic N was observed, whereas the change for graphitic N was less pronounced. These results clearly substantiate the changes in the coordination environment of the Ru SAC catalytic sites, especially an increased
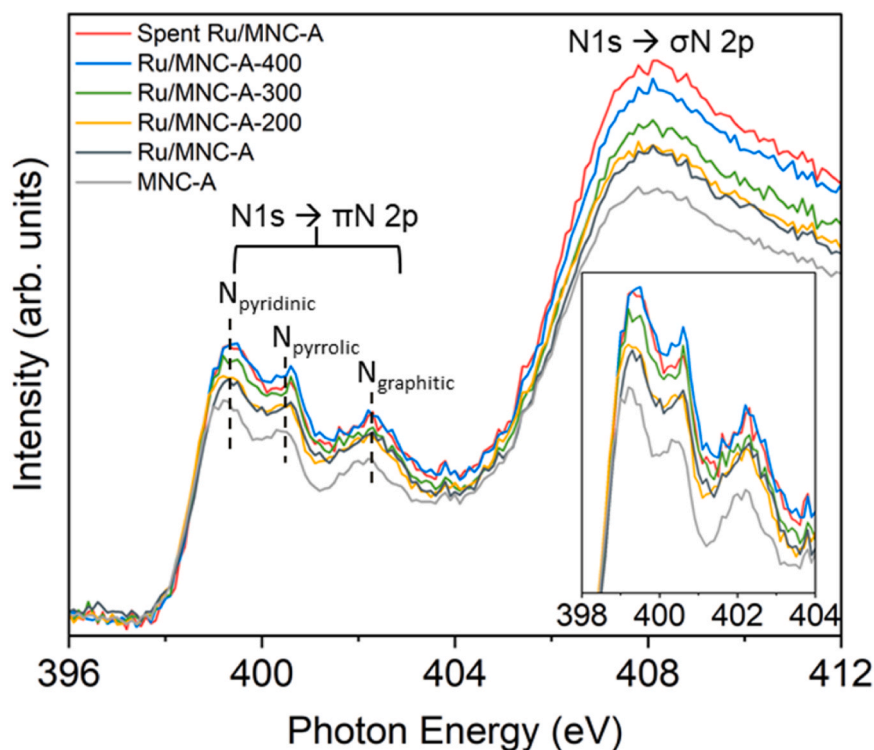
Fig. 9. Comparative N K-edge NEXAFS analysis of Ru/MNC-A, spent Ru/MNC-A, and reduced samples at different temperatures.

level of interaction between Ru and the pyridinic N and pyrrolic N sites under the reductive condition [42–45]. In particular, Ru/MNC-A-400 and spent Ru/MNC-A presented very similar spectral features, implying that preliminary thermal treatment results in near-identical local coordination environments for the active sites. Complementing these findings, the TEM image in Fig. S18 exhibited an isolated dispersion of Ru SACs in the Ru/MNC-A-400 even after the reduction process. Besides, the EXAFS analysis for Ru/MNC-A-400 revealed that a bond distance of 1.6 Å and coordination number 3 are consistently maintained (Fig. S19, S20, and Table S8). Notably, there was no evidence of a Ru-Ru bond generation at a distance of 2.3 Å, further indicating that the Ru SAC state remains intact during the reduction process. This phenomenon aligns with observations from prior studies, which suggest that under high-temperature or reductive conditions, nanoparticles can undergo redispersion into single atoms, and single atoms are capable of migrating across the catalyst support surface [46,47]. Such dynamic behavior is crucial for the catalytic efficiency of SACs, as it influences the dispersion and stability of the active sites. Consequently, we envisage that under the reductive thermal treatment, Ru catalysts in active sites supported on MNC-A move from weak binding sites to stronger ones like pyridinic N and pyrrolic N sites, while retaining their inherent SAC properties.

We theoretically corroborated our experimental observations and ascertained the hypothesized migration of Ru single atoms from weakly binding sites (either graphene or graphitic-N) to more robust anchoring sites (either pyridinic-N or pyrrolic-N) upon thermal treatment by using density functional theory (DFT) calculation. Our calculations employed a large 10×10 supercell graphene surface containing 200 carbon atoms to negate inter-periodic cell interactions. To simulate the N-doped carbon supports probed experimentally, nitrogen was substituted at defect sites of pristine graphene, yielding graphitic-N, pyridinic-N, and pyrrolic-N structures. Moreover, to represent the actual N-doped carbon structure confirmed from the EXAFS data, the pyridinic-N3 and pyrrolic-pyridinic-N2 structure was designed for the DFT calculation (Fig. S21).

The adsorption behavior of Ru single atoms on these relaxed surfaces was then studied using the conditions outlined in the experimental

session. Fig. S22 and Table S13 detail the adsorption structures and binding energies for each model. Notably, Ru single atoms were found at hole sites where they can interact with neighboring carbon atoms on the surface. The bonding energy of Ru on pyridinic-N3 and pyrrolic-pyridinic-N2 were calculated to be -6.42 eV and -6.18 eV, respectively, significantly higher than the energy on graphene and graphitic-N (-3.05 eV and -2.81 eV, respectively). Interestingly, the adsorption energy on pyridinic-N3 and pyrrolic-pyridinic-N2 was about two times higher than that on graphene and graphitic-N, which was consistent with previous literature [19]. This reaffirms the experimental observation that Ru single atoms preferentially anchor to pyridinic-N and pyrrolic-N sites during metalation.

We probed the migration behavior and associated energy requirements for Ru migration on the simulated surfaces using the CI-NEB method. Two diffusion paths linking to another hole (C6) site on graphene were investigated. We disregarded adsorption at atop (C1) and bridge (C2) sites since their adsorption stability was found inferior to that at the hole sites. The first diffusion route involves the hole-bridge-hole trajectory, whereas the alternate course takes the hole-atop-bridge-atop-hole route, both depicted in the right panel of Fig. 10a. Data from Fig. 10a and Table S14 indicate that Ru single atoms on graphene necessitate less than 1 eV of energy for migration. Remarkably, the energy required along either pathway was comparable, suggesting that upon sufficient energy input, Ru on graphene can navigate in any chosen direction. The calculated relative energy at each stage during the Ru diffusion on graphitic-N is detailed in Fig. 10b. We examined two possible pathways. One that involves the hole site and another that features an alternate graphitic-N site. It emerged that the activation energy needed for migrating a Ru single atom anchored to a graphitic-N site is below 1 eV. This suggests that the graphitic-N surface may not adequately stabilize Ru, especially when external energy induced into the single atom catalyst anchored to the graphitic-N site. Crucially, the activation energy for Ru diffusion to site 1 and the relative energy at the final image were found to be 0.14 eV and -0.36 eV, respectively. This implies a weaker adsorption strength of the Ru atom on graphitic-N compared to graphene, further hinting at the enhanced mobility of Ru
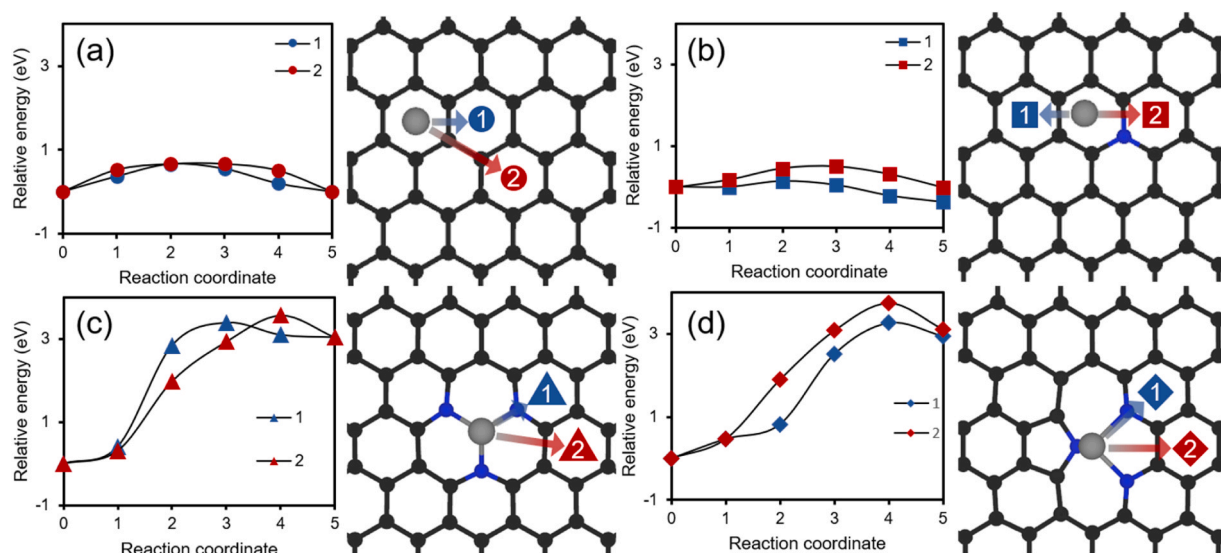
Fig. 10. Relative energy of each reaction coordinated calculated by CI-NEB method and schematic illustration during the migration of Ru single atom adsorbed on graphene (a), graphitic-N (b), pyridinic-N_3 (c), and pyrrolic-pyridinic-N_2 (d) surface to the symbolized anchoring site. The black, blue and grey sphere indicate the carbon, nitrogen and ruthenium atom, respectively.

single atoms on the graphitic-N surface.

On the other hand, Ru migration on the pyridinic-N_3 surface exhibited a different relative energy trend. On the pyridinic-N_3 surface, two kinds of movement pathway of Ru single atom were considered (Fig. 10c). When the Ru atom anchored on the pyridinic-N_3 site migrated to an alternate site, the relative energy at the final step significantly exceeded that of the initial structure, with a difference higher than 3 eV. The activation energy required for Ru atom migration on pyridinic-N surpassed 3.57 eV, a value six-fold higher than that on graphene or graphitic-N surfaces. Similarly, migration energy trends for Ru on the pyrrolic-pyridinic-N_2 surface mirrored those on the pyridinic-N_3. As illustrated in Fig. 10d, the relative adsorption energy for Ru migrating to two distinct hole sites reached 3 eV, with activation energies approximately six times that on graphene. The markedly elevated activation energy suggests a higher energy demand for Ru atom diffusion on the other sites when Ru single atom adsorbed on the pyridinic or pyrrolic-N site. Consequently, the significantly increased activation energies for migration on pyridinic-N_3 and pyrrolic-pyridinic-N_2 surfaces denote depressed mobility of Ru atoms. In contrast, on graphene and graphitic-N surfaces, Ru demonstrated greater mobility, relocating with ease to different anchoring sites when adequate energy was supplied. In light of these computational insights, it is anticipated that the predominant adsorption of Ru single atoms will be on the pyridinic-N and pyrrolic-N sites rather than graphene or graphitic-N. This conclusion aligns seamlessly with our previously detailed experimental observations.

A comparative evaluation of Ru/MNC-A-400 and pristine Ru/MNC-A revealed a clear difference in the catalytic stability throughout the recycling tests (Fig. 11a and Table S15). The Ru/MNC-A-400 retained ~85% of its initial catalytic activity by the fifth cycle. Ru leaching was substantially mitigated in the thermally pretreated catalyst, and ~96% of the initial Ru content was sustained after five cycles. Comprehensive analyses using HAADF-STEM, XPS, and XAS indicated only minor differences in aspects such as the dispersion, oxidation state, and binding environment of Ru in the spent Ru/MNC-A-400 catalyst (Fig. S19 and S23-25). Corroborated by the NEXAFS analysis, the observed enhancements are attributed to intensified interaction between the support and Ru SACs because the migration and rearrangement of the Ru species at neighboring N sites with stronger binding affinities occurs during the reductive thermal process. However, loosely bound Ru can exhibit a higher activity than the strongly bound Ru species, which is consistent with our previous reports on Ru SACs supported on N-doped carbon supports [17].
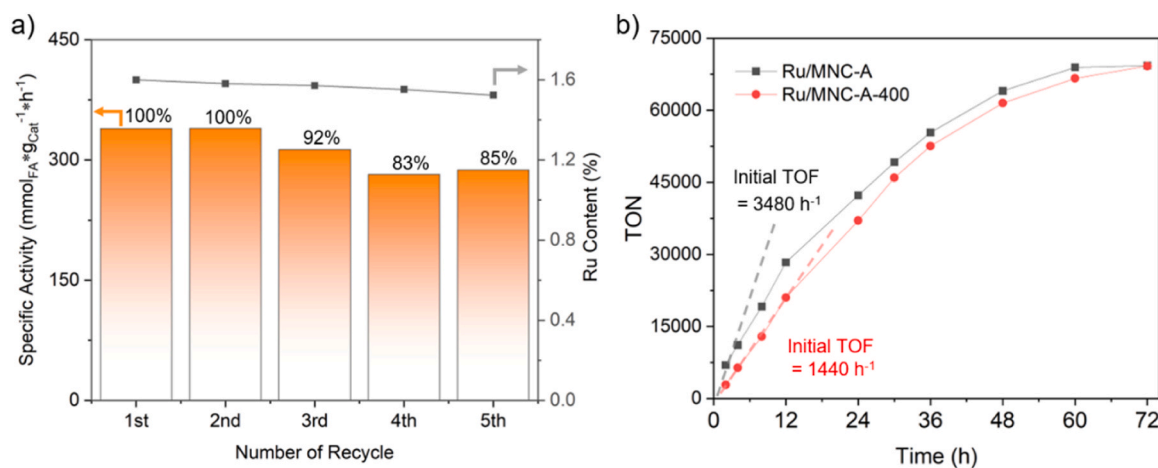
Fig. 11. Evaluation of the recyclability (a) and comparative time-dependent reaction of Ru/MNC-A-400 with its pristine analog (b).

Conclusively, the decrease in activity observed during the recycling tests of Ru/MNC-A cannot be attributed to the physical/chemical degradation of the support structure or changes in the properties of the Ru SAC. Instead, it is due to the rearrangement of the weakly bound Ru species to more strongly binding sites under the reducing conditions. This, in turn, imparts excellent stability to the catalyst during the conversion of CO_2 to formate under reductive conditions. Moreover, to further verify the outstanding stability of these catalysts, time-dependent hydrogenation was conducted at a high substrate to Ru catalyst ratio. Fig. 11b visually documents a steady increase in the TON over 72 h in the hydrogenation of CO_2 to formate, driven by both Ru/MNC-A and Ru/MNC-A400 catalysts. This result also reveals that the pristine catalyst has a faster reaction rate in the initial reaction stages. Significantly, the Ru/MNC-A catalyst exhibited exceptional catalytic activity, comparable to many of the catalyst systems recently reported for CO_2 hydrogenation (Table S16). Its superior stability was particularly noteworthy, achieving a TON of 315,840 in a prolonged reaction duration of 360 h (Table S17 and Fig. S26). This finding compellingly demonstrates the remarkable stability of the catalyst, which can be attributed to the robustly anchored Ru SACs on the MNC-A support.

4. Conclusion

This study focused on the fabrication and characterization of MNCs using different precursors and their subsequent application as supports for immobilizing Ru catalysts for the hydrogenation of CO_2 to formate. The successful formation of mesoporous structures in the synthesized MNC supports through the replication of the cubic Ia3d structure from the KIT-6 template was confirmed. However, MNC-M obtained using melamine as the precursor did not exhibit discernible crystalline peaks, indicating the absence of an ordered mesoporous structure. Further, the nitrogen content and chemical states of N sites in the MNCs were demonstrated to differ according to the precursor used. Remarkably, the synergistic effect of the nitrogen content, chemical states of N dopants, and well-defined 3D mesoporous structures significantly affected the stability of the supported Ru SACs under the reaction conditions. Particularly, the recyclability of the different catalysts varied, with Ru/MNC-A demonstrating the best stability, whereas Ru/MC-S-im and Ru/MNC-P exhibited decreased activity after multiple cycles due to severe Ru agglomeration. Ru/MNC-M exhibited low activity due to limited reactant diffusion caused by its small pore widths. Considering the distinct properties of Ru/MNC-A, the observed decline in its activity during the recycling tests was not due to intrinsic changes in the support structure or the Ru SAC characteristics. As corroborated by the NEXAFS analysis, the migration and repositioning of Ru to adjacent nitrogen sites with stronger binding affinities under the reductive thermal process resulted in intensified interaction between the support and Ru SACs. This rearrangement phenomenon imparted Ru/MNC-A a remarkable stability in the hydrogenation of CO_2 to formate, even under reductive conditions. Thus, both the Ru/MNC-A and Ru/MNC-A400 catalysts exhibited superior performance in time-dependent CO_2 hydrogenation to formate, achieving a remarkable TON of ~69,000 with an acid-to-amine ratio of 0.61 in 72 h. Impressively, the Ru/MNC-A catalyst showcased outstanding stability, achieving an impressive TON of 315,840 across an extended period of 360 h. This research highlights the importance of the mesoporous structure and nitrogen dopants in support materials in stabilizing ruthenium SACs during CO_2 hydrogenation to formate. These findings provide valuable insights for the design and development of highly stable and efficient Ru SACs for various catalytic applications, contributing to the advancement of sustainable carbon dioxide utilization. Further exploration into optimizing the pore structure and nitrogen-doping strategies could further enhance the performance of the Ru SACs and expand their potential in catalysis.

CRediT authorship contribution statement

Jung Kwang-Deog: Conceptualization, Funding acquisition, Project administration, Resources, Supervision, Writing – review & editing. **Van Canh Nguyen:** Data curation, Investigation, Validation. **Ahn Sunghee:** Data curation, Investigation, Validation, Writing – original draft. **Lee Kyung Rok:** Conceptualization, Data curation, Formal analysis, Investigation, Methodology, Validation, Visualization, Writing – original draft, Writing – review & editing. **Park Kwangho:** Conceptualization, Data curation, Formal analysis, Investigation, Methodology, Validation, Visualization, Writing – original draft, Writing – review & editing.

Declaration of Competing Interest

The authors declare that they have no known competing financial interests or personal relationships that could have appeared to influence the work reported in this paper.

Data Availability

No data was used for the research described in the article.

Acknowledgments

Appendix A. Supporting information

Supplementary data associated with this article can be found in the online version at doi:10.1016/j.apcatb.2024.123751.

References

[1] K. Sordakis, C. Tang, L.K. Vogt, H. Junge, P.J. Dyson, M. Beller, G. Laurenczy, Homogeneous catalysis for sustainable hydrogen storage in formic acid and alcohols, Chem. Rev. 118 (2018) 372–433, https://doi.org/10.1021/acs.chemrev.7b00182.

[2] W.-H. Wang, Y. Himeda, J.T. Muckerman, G.F. Manbeck, E. Fujita, CO_2 hydrogenation to formate and methanol as an alternative to photo-and electrochemical CO_2 reduction, Chem. Rev. 115 (2015) 12936–12973, https://doi.org/10.1021/acs.chemrev.5b00197.

[3] A. Álvarez, A. Bansode, A. Urakawa, A.V. Bavykina, T.A. Wezendonk, M. Makkee, J. Gascon, F. Kapteijn, Challenges in the greener production of formates/formic acid, methanol, and DME by heterogeneously catalyzed CO_2 hydrogenation processes, Chem. Rev. 117 (2017) 9804–9838, https://doi.org/10.1021/acs.chemrev.6b00816.

[4] D. Liu, Q. He, S. Ding, L. Song, Structural regulation and support coupling effect of single-atom catalysts for heterogeneous catalysis, Adv. Energy Mater. 10 (2020) 2001482, https://doi.org/10.1002/aenm.202001482.

[5] J. Hao, Z. Zhuang, K. Cao, G. Gao, C. Wang, F. Lai, S. Lu, P. Ma, W. Dong, T. Liu, M. Du, H. Zhu, Unraveling the electronegativity-dominated intermediate adsorption on high-entropy alloy electrocatalysts, Nat. Commun. 13 (2022) 2662, https://doi.org/10.1038/s41467-022-30379-4.

[6] J. Hao, H. Zhu, Q. Zhao, J. Hao, S. Lu, X. Wang, F. Duan, M. Du, Interatomic electron transfer promotes electroreduction CO_2-to-CO efficiency over a CuZn diatomic site, Nano Res. 16 (2023) 8863–8870, https://doi.org/10.1007/s12274-023-5577-2.

[7] H. Zhu, J. Hu, Z. Zhang, Z. Zhuang, J. Hao, F. Duan, S. Lu, X. Wang, M. Du, Lewis acid sites incorporation promotes CO_2 electroreduction to multicarbon oxygenates over B-CuO nanotubes, Appl. Catal. B-Environ. 339 (2023) 123082, https://doi.org/10.1016/j.apcatb.2023.123082.

[8] K. Park, G.H. Gunasekar, N. Prakash, K.D. Jung, S. Yoon, A highly efficient heterogenized iridium complex for the catalytic hydrogenation of carbon dioxide

to formate, ChemSusChem 8 (2015) 3410–3413, https://doi.org/10.1002/cssc.201500436.

[9] G.H. Gunasekar, K. Park, V. Ganesan, K. Lee, N.-K. Kim, K.-D. Jung, S. Yoon, A covalent triazine framework, functionalized with Ir/N-heterocyclic carbene sites, for the efficient hydrogenation of CO₂ to formate, Chem. Mater. 29 (2017) 6740–6748, https://doi.org/10.1021/acs.chemmater.7b01539.

[10] G.H. Gunasekar, J. Shin, K.-D. Jung, K. Park, S. Yoon, Design strategy toward recyclable and highly efficient heterogeneous catalysts for the hydrogenation of CO₂ to formate, ACS Catal. 8 (2018) 4346–4353, https://doi.org/10.1021/acscatal.8b00392.

[11] G.H. Gunasekar, D. Hyun, P. Natarajan, K.-D. Jung, S. Yoon, An effective heterogeneous Ir(III) catalyst, immobilized on a heptazine-based organic framework, for the hydrogenation of CO₂ to formate, Catal. Today 265 (2016) 52–55, https://doi.org/10.1016/j.cattod.2015.10.037.

[12] A. Kann, H. Hartmann, A. Besmehn, P.J. Hausoul, R. Palkovits, Hydrogenation of CO₂ to formate over ruthenium immobilized on solid molecular phosphines, ChemSusChem 11 (2018) 1857–1865, https://doi.org/10.1002/cssc.201800413.

[13] X. Shao, X. Yang, J. Xu, S. Liu, S. Miao, X. Liu, X. Su, H. Duan, Y. Huang, T. Zhang, Iridium single-atom catalyst performing a quasi-homogeneous hydrogenation transformation of CO₂ to formate, Chem 5 (2019) 693–705, https://doi.org/10.1016/j.chempr.2018.12.014.

[14] A. Jaleel, S.-H. Kim, P. Natarajan, G.H. Gunasekar, K. Park, S. Yoon, K.-D. Jung, Hydrogenation of CO₂ to formates on ruthenium(III) coordinated on melamine polymer network, J. CO₂ Util. 35 (2020) 245–255, https://doi.org/10.1016/j.jcou.2019.10.003.

[15] G.H. Gunasekar, S. Yoon, A phenanthroline-based porous organic polymer for the iridium-catalyzed hydrogenation of carbon dioxide to formate, J. Mater. Chem. A. 7 (2019) 14019–14026, https://doi.org/10.1039/C9TA03807H.

[16] H. Park, K. Park, K.-D. Jung, S. Yoon, CO₂ hydrogenation into formate and methyl formate using Ru molecular catalysts supported on NNN pincer porous organic polymers, Inorg. Chem. Front. 8 (2021) 1727–1735, https://doi.org/10.1039/D0QI01123A.

[17] B. Chen, M. Dong, S. Liu, Z. Xie, J. Yang, S. Li, Y. Wang, J. Du, H. Liu, B. Han, CO₂ hydrogenation to formate catalyzed by Ru coordinated with a N, P-containing polymer, ACS Catal. 10 (2020) 8557–8566, https://doi.org/10.1021/acscatal.0c01678.

[18] K. Park, G.H. Gunasekar, S.-H. Kim, H. Park, S. Kim, K. Park, K.-D. Jung, S. Yoon, CO₂ hydrogenation to formic acid over heterogenized ruthenium catalysts using a fixed bed reactor with separation units, Green. Chem. 22 (2020) 1639–1649, https://doi.org/10.1039/C9GC03685G.

[19] A. Jaleel, A. Haider, C.Van Nguyen, K.R. Lee, S. Choung, J.W. Han, S.-H. Baek, C.-H. Shin, K.-D. Jung, Structural effect of nitrogen/carbon on the stability of anchored Ru catalysts for CO₂ hydrogenation to formate, Chem. Eng. J. 433 (2022) 133571, https://doi.org/10.1016/j.cej.2021.133571.

[20] S. Ahn, K. Park, K.R. Lee, A. Haider, C.Van Nguyen, H. Jin, S.J. Yoo, S. Yoon, K.-D. Jung, Atomically dispersed Ru(III) on N-doped mesoporous carbon hollow spheres as catalysts for CO₂ hydrogenation to formate, Chem. Eng. J. 442 (2022) 136185, https://doi.org/10.1016/j.cej.2022.136185.

[21] W. Wang, S. Wang, X. Ma, J. Gong, Recent advances in catalytic hydrogenation of carbon dioxide, Chem. Soc. Rev. 40 (2011) 3703–3727, https://doi.org/10.1039/C1CS15008A.

[22] G.H. Gunasekar, K. Park, K.-D. Jung, S. Yoon, Recent developments in the catalytic hydrogenation of CO₂ to formic acid/formate using heterogeneous catalysts, Inorg. Chem. Front. 3 (2016) 882–895, https://doi.org/10.1039/C5QI00231A.

[23] R. Sun, Y. Liao, S.-T. Bai, M. Zheng, C. Zhou, T. Zhang, B.F. Sels, Heterogeneous catalysts for CO₂ hydrogenation to formic acid/formate: from nanoscale to single atom, Energy Environ. Sci. 14 (2021) 1247–1285, https://doi.org/10.1039/D0EE03575K.

[24] A.V. Bavykina, E. Rozhko, M.G. Goesten, T. Wezendonk, B. Seoane, F. Kapteijn, M. Makkee, J. Gascon, Shaping covalent triazine frameworks for the hydrogenation of carbon dioxide to formic acid, ChemCatChem 8 (2016) 2217–2221, https://doi.org/10.1002/cctc.201600419.

[25] A.V. Bavykina, A.I. Olivos-Suarez, D. Osadchii, R. Valecha, R. Franz, M. Makkee, F. Kapteijn, J. Gascon, Facile method for the preparation of covalent triazine framework coated monoliths as catalyst support: applications in C1 catalysis, ACS Appl. Mater. Interfaces 9 (2017) 26060–26065, https://doi.org/10.1021/acsami.7b07339.

[26] Y. Kuwahara, Y. Fujie, H. Yamashita, Poly(ethyleneimine)-tethered Ir complex catalyst immobilized in titanate nanotubes for hydrogenation of CO₂ to formic acid, ChemCatChem 9 (2017) 1906–1914, https://doi.org/10.1002/cctc.201700508.

[27] H.K. Lo, C. Copéret, CO₂ hydrogenation to formate with immobilized Ru-catalysts based on hybrid organo-silica mesostructured materials, ChemCatChem 11 (2019) 430–434, https://doi.org/10.1002/cctc.201801368.

[28] H.K. Lo, I. Thiel, C. Copéret, Efficient CO₂ hydrogenation to formate with immobilized Ir-catalysts based on mesoporous silica beads, Eur. J. Chem. 25 (2019) 9443–9446, https://doi.org/10.1002/chem.201901663.

[29] A.H. Lu, F. Schüth, Nanocasting: a versatile strategy for creating nanostructured porous materials, Adv. Mater. 18 (2006) 1793–1805, https://doi.org/10.1002/adma.200600148.

[30] Z. Liu, Y. Du, P. Zhang, Z. Zhuang, D. Wang, Bringing catalytic order out of chaos with nitrogen-doped ordered mesoporous carbon, Matter 4 (2021) 3161–3194, https://doi.org/10.1016/j.matt.2021.07.019.

[31] Q. Shen, H. Jin, P. Li, X. Yu, L. Zheng, W. Song, C. Cao, Breaking the activity limitation of iridium single-atom catalyst in hydrogenation of quinoline with synergistic nanoparticles catalysis, Nano Res. 15 (2022) 5024–5031, https://doi.org/10.1007/s12274-022-4235-4.

[32] Y. Zhang, Y. Wu, Y. Su, Y. Cao, Z. Liang, D. Yang, R. Yu, D. Zhang, J. Wu, W. Xiao, In situ synthesis of CuN₄/mesoporous N-doped carbon for selective oxidative crosscoupling of terminal alkynes under mild conditions, Small 18 (2022) 2105178, https://doi.org/10.1002/smll.202105178.

[33] T.-W. Kim, F. Kleitz, B. Paul, R. Ryoo, MCM-48-like large mesoporous silicas with tailored pore structure: facile synthesis domain in a ternary triblock copolymer–butanol–water system, J. Am. Chem. Soc. 127 (2005) 7601–7610, https://doi.org/10.1021/ja042601m.

[34] K.S. Sing, Reporting physisorption data for gas/solid systems with special reference to the determination of surface area and porosity (Recommendations 1984), Pure Appl. Chem. 57 (1985) 603–619, https://doi.org/10.1351/pac198557040603.

[35] K.P. Gierszal, T.-W. Kim, R. Ryoo, M. Jaroniec, Adsorption and structural properties of ordered mesoporous carbons synthesized by using various carbon precursors and ordered siliceous *P6mm* and *Ia3̄d* mesostructures as templates, J. Phys. Chem. B. 109 (2005) 23263–23268, https://doi.org/10.1021/jp054562m.

[36] A. Lu, A. Kiefer, W. Schmidt, F. Schüth, Synthesis of polyacrylonitrile-based ordered mesoporous carbon with tunable pore structures, Chem. Mater. 16 (2004) 100–103, https://doi.org/10.1021/cm031095h.

[37] C.-M. Yang, C. Weidenthaler, B. Spliethoff, M. Mayanna, F. Schüth, Facile template synthesis of ordered mesoporous carbon with polypyrrole as carbon precursor, Chem. Mater. 17 (2005) 355–358, https://doi.org/10.1021/cm049164v.

[38] M. Lezanska, J. Wloch, G. Szymański, I. Szpakowska, J. Kornatowski, Properties of CMK-8 carbon replicas obtained from KIT-6 and pyrrole at various contents of ferric catalyst, Catal. Today 150 (2010) 77–83, https://doi.org/10.1016/j.cattod.2009.06.020.

[39] Y. Yao, B. Zhang, J. Shi, Q. Yang, Preparation of nitrogen-doped carbon nanotubes with different morphologies from melamine-formaldehyde resin, ACS Appl. Mater. Interfaces 7 (2015) 7413–7420, https://doi.org/10.1021/acsami.5b01233.

[40] D.J. Morgan, Resolving ruthenium: XPS studies of common ruthenium materials, Surf. Interface Anal. 47 (2015) 1072–1079.

[41] X. Wang, W. Chen, L. Zhang, T. Yao, W. Liu, Y. Lin, H. Ju, J. Dong, L. Zheng, W. Yan, Uncoordinated amine groups of metal–organic frameworks to anchor single Ru sites as chemoselective catalysts toward the hydrogenation of quinoline, J. Am. Chem. Soc. 139 (2017) 9419–9422.

[42] R. Arrigo, M.E. Schuster, Z. Xie, Y. Yi, G. Wowsnick, L.L. Sun, K.E. Hermann, M. Friedrich, P. Kast, M. Hävecker, Nature of the N–Pd interaction in nitrogen-doped carbon nanotube catalysts, ACS Catal. 5 (2015) 2740–2753.

[43] D.A. Bulushev, M. Zacharska, E.V. Shlyakhova, A.L. Chuvilin, Y. Guo, S. Beloshapkin, A.V. Okotrub, L.G. Bulusheva, Single isolated Pd2+ cations supported on N-doped carbon as active sites for hydrogen production from formic acid decomposition, ACS Catal. 6 (2016) 681–691.

[44] L. Cao, Q. Luo, J. Chen, L. Wang, Y. Lin, H. Wang, X. Liu, X. Shen, W. Zhang, W. Liu, Dynamic oxygen adsorption on single-atomic Ruthenium catalyst with high performance for acidic oxygen evolution reaction, Nat. Commun. 10 (2019) 4849.

[45] A. Iemhoff, M. Vennewald, J. Artz, C. Mebrahtu, A. Meledin, T.E. Weirich, H. Hartmann, A. Besmehn, M. Aramini, F. Venturini, On the stability of isolated iridium sites in N-rich frameworks against agglomeration under reducing conditions, ChemCatChem 14 (2022) e202200179.

[46] J. Hao, Z. Zhuang, J. Hao, C. Wang, S. Lu, F. Duan, F. Xu, M. Du, H. Zhu, Interatomic electronegativity offset dictates selectivity when catalyzing the CO₂ reduction reaction, Adv. Energy Mater. 12 (2022) 2200579, https://doi.org/10.1002/aenm.202200579.

[47] J. Hao, H. Zhu, Z. Zhuang, Q. Zhao, R. Yu, J. Hao, Q. Kang, S. Lu, X. Wang, J. Wu, D. Wang, M. Du, Competitive trapping of single atoms onto a metal carbide surface, ACS Nano 17 (2023) 6955–6965, https://doi.org/10.1021/acsnano.3c00866.